

# **Heavy Fluorination via Ion Exchange Achieves** High-Performance Li-Mn-O-F Layered Cathode for Li-Ion Batteries

Junliang Lu, Bo Cao, Bingwen Hu, Yuxin Liao, Rui Qi, Jiajie Liu, Changjian Zuo, Shenyang Xu, Zhibo Li, Cong Chen, Mingjian Zhang,\* and Feng Pan

Lithium-excess manganese layered oxide Li<sub>2</sub>MnO<sub>3</sub>, attracts much attention as a cathode in Li-ion batteries, due to the low cost and the ultrahigh theoretical capacity (≈460 mA h g<sup>-1</sup>). However, it delivers a low reversible practical capacity (<200 mA h g<sup>-1</sup>) due to the irreversible oxygen redox at high potentials (>4.5 V). Herein, heavy fluorination (9.5%) is successfully implemented in the layered anionic framework of a Li-Mn-O-F (LMOF) cathode through a unique ion-exchange route. F substitution with O stabilizes the layered anionic framework, completely inhibits the O2 evolution during the first cycle, and greatly enhances the reversibility of oxygen redox, delivering an ultrahigh reversible capacity of 389 mA h g<sup>-1</sup>, which is 85% of the theoretical capacity of Li<sub>2</sub>MnO<sub>3</sub>. Moreover, it also induces a thin spinel shell coherently forming on the particle surface, which greatly improves the surface structure stability, making LMOF exhibit a superior cycling stability (a capacity retention of 91.8% after 120 cycles at 50 mA g<sup>-1</sup>) and excellent rate capability. These findings stress the importance of stabilizing the anionic framework in developing high-performance low-cost cathodes for next-generation Li-ion batteries.

1. Introduction

Lithium-ion batteries (LIBs) have been widely applied in 3C electronic products, electric vehicles, and the massive-scale energy storage systems.<sup>[1]</sup> In the past few decades, tremendous efforts had been devoted studying high energy density cathode materials,<sup>[2]</sup> such as layered LiCoO<sub>2</sub> (≈150 mA h g<sup>-1</sup>),  $\text{LiNi}_x \text{Mn}_y \text{Co}_{1-x-y} \text{O}_2$  (NMC,  $\approx 200 \text{ mA h g}^{-1}$ ) and Li-rich cathode materials  $xLi_2MnO_3 \cdot yLiTMO_2$  (TM = Mn, Co, Ni, etc.; ≈250 mA h g<sup>-1</sup>).<sup>[3]</sup> Especially, Li-rich cathode materials are

J. Lu, B. Cao, R. Qi, J. Liu, C. Zuo, S. Xu, Z. Li, C. Chen, M. Zhang, F. Pan School of Advanced Materials

Peking University

Shenzhen Graduate School Shenzhen 518055, China E-mail: zhangmj@pkusz.edu.cn

B. Hu, Y. Liao

Shanghai Key Laboratory of Magnetic Resonance State Key Laboratory of Precision Spectroscopy School of Physics and Electronic Science East China Normal University Shanghai 200241, China

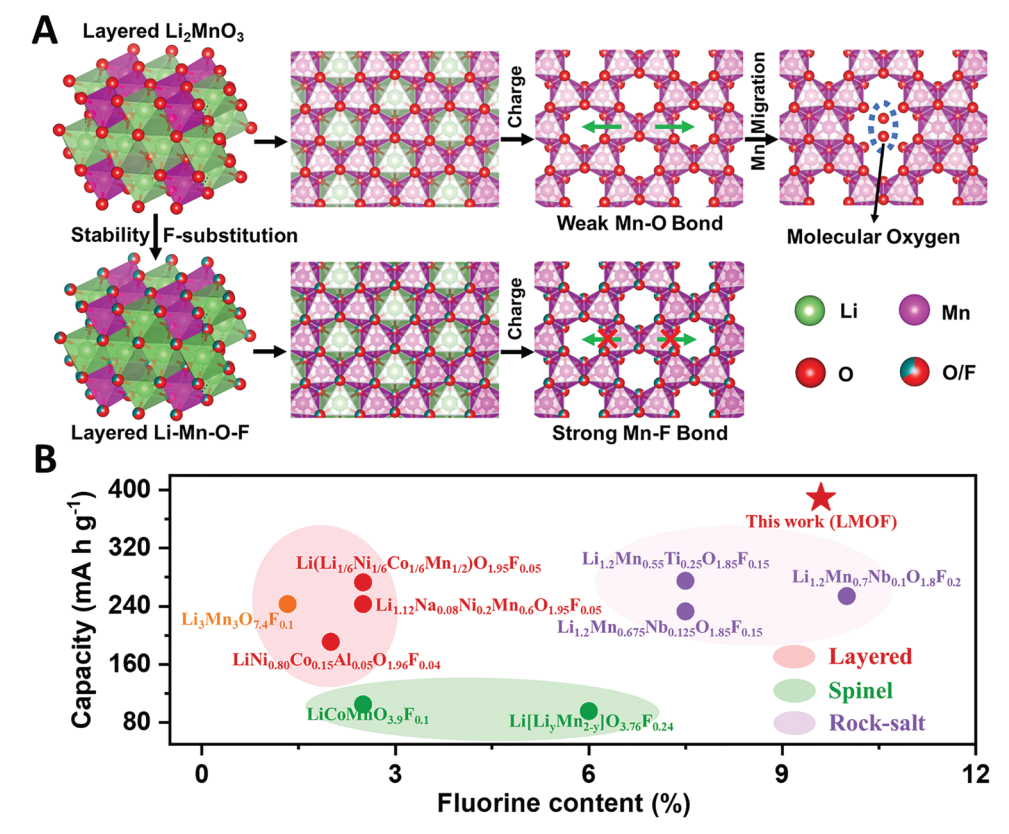
The ORCID identification number(s) for the author(s) of this article can be found under https://doi.org/10.1002/smll.202103499.

DOI: 10.1002/smll.202103499

considered as the promising candidate cathodes for the next-generation LIBs because of its high reversible capacity, and the low cost compared with LiCoO<sub>2</sub> and NMC.[4] As the parent material of Li-rich cathodes, Li<sub>2</sub>MnO<sub>3</sub> has attracted much attention due to the low cost, the environmental friendliness, and the high theoretical capacity (≈460 mA h g<sup>-1</sup>). Nevertheless, it suffers from low practical capacity, and poor cyclic stability.[4a] The root cause can be ascribed to the inevitable oxygen evolution during the first charge, which results into the irreversible oxygen redox,<sup>[5]</sup> and severe structural degradation from layered to spinel phase due to TM migration (top panel of **Scheme 1**A).<sup>[5–6]</sup> Therefore, enhancing the stability of layered anionic framework is the crucial way toward high-performance Li-Mn-O layered oxide cathodes.

Up to now, multiple strategies have been demonstrated effective in improving the performance of Li-rich layered oxide cathodes, including surface modification using oxide materials (TiO2, Co3O4, and NiO) and reduced graphene oxide (rGO),[7] element doping by cations (Mg, Al, Ti, V, Ni, Cr, etc.) and anions (P and F),[8] and nanostructure design such as nanowire, nanobelts, nanoplates, etc.<sup>[9]</sup> Among these strategies, F doping has been widely used and exhibited great advantages in improving the electrochemical performance of Li-rich layered oxide cathodes and beyond (Tables S1 and S2, Supporting Information). Dong et al. reported that F substitution could improve the conductivity of Li+/electron by weakening Li-O bonds and inducing more Mn3+ and oxygen vacancies.<sup>[8i]</sup> Lun et al. demonstrated that F doping not only reduced irreversible oxygen redox and oxygen loss, but also diminished the Mn<sup>3+</sup>-induced Jahn–Teller distortion to improve the capacity retention. [10] As we know, Mn-F bond has a stronger bond dissociation energy (423 kJ mol<sup>-1</sup>) than Mn-O bond (402 kJ mol<sup>-1</sup>).<sup>[11]</sup> Thus strong Mn-F bond can inhibit Mn migration in TM layers, then suppress the formation of molecular O2, and increase the stability of the oxygen framework (lower panel of Scheme 1A). To make full advantage of F substitution, high F doping content is necessary. However, due to the limited fluorine solubility into oxides, the traditional high-temperature calcination can only dope F content below 3% in the layered oxides (Scheme 1B). Further increasing the

16136282, 2022, 6, Downloaded from https://onlinelibrary.wiley.com/doi/10.1002/smll.202103499 by University Town of Shenzlen, Wiley Online Library on [24110205]. See the Terms and Conditions (https://onlinelibrary.wiley.com/terms-and-conditions) on Wiley Online Library for rules of use; OA articles are governed by the applicable Creative Commons Licenses, and Conditions (https://onlinelibrary.wiley.com/terms-and-conditions) on Wiley Online Library for rules of use; OA articles are governed by the applicable Creative Commons Licenses, and Conditions (https://onlinelibrary.wiley.com/terms-and-conditions) on Wiley Online Library for rules of use; OA articles are governed by the applicable Creative Commons Licenses, and Conditions (https://onlinelibrary.wiley.com/terms-and-conditions) on Wiley Online Library for rules of use; OA articles are governed by the applicable Creative Commons Licenses, and Conditions (https://onlinelibrary.wiley.com/terms-and-conditions) on Wiley Online Library for rules of use; OA articles are governed by the applicable Creative Commons Licenses, and the common of the



Scheme 1. A) Schematic diagram of the design route for the Li-Mn-O-F layered cathode material with the low cost, high capacity and good stability. B) An overview of F doping oxide cathode materials for LIBs synthesized by the calcination method.

F content would induce the phase transformation from the layered oxides to the spinel phase even rock salt phase, which possess the lower capacity or much poor cycling stability and rate capacity. By means of mechanical milling, a higher F content, even >30%, can be implemented in the rock-salt oxides (Table S2, Supporting Information).<sup>[12]</sup> To the best of our knowledge, there is no route reported to implement heavy F substitution in layered oxides.

In this study, a cathode material  $\text{Li}_{0.87}\text{Mn}_{0.80}\text{O}_{1.81}\text{F}_{0.19}$  (LMOF) with heavy F doping (9.5%) was synthesized through a unique ion exchange method. Such a heavy F substitution not only greatly enhances the reversibility of anionic redox in the bulk structure, but also stabilizes the surface structure by inducing the formation of a uniform spinel shell on the particle surface. This material showed ultra-high discharge capacity (389 mA h g<sup>-1</sup>), the reduced average voltage decay (<2 mV per cycle) and superior cycle stability (91.8% after 120 cycles at 50 mA g<sup>-1</sup>). These findings provide new routes to develop high performance layered oxide cathodes for Li-ion batteries through high concentration anionic substitution.

### 2. Results and Discussion

LMOF sample was prepared from a Na-containing precursor NLMOF using Li/Na-ion exchange method (see details in the Experimental Section in the Supporting Information). X-ray diffraction (XRD) patterns of NLMOF and LMOF were taken

to examine the crystalline structures (Figure 1A,B). The phase analysis reveals that, NLMOF is a composite consisting of three components, including P3-type Na-containing layered oxide (S. G. R3m).

Li<sub>2</sub>MnO<sub>3</sub> (S. G. C2/m) and NaF. Rietveld refinement deduces their weight ratios as 81.26%, 8.18%, and 10.57%, respectively. So high content of NaF indicates that, there is a little amount of F entering the lattice of layered oxides during the synthesis of NLMOF. After ion-exchange, LMOF is composed of two phases, layered phase (S. G. R-3m) and spinel phase (S. G. Fd-3m). The corresponding weight percentage were 86.56% and 13.44%, respectively. The detailed refinement results were deposited in Tables S3 and S4 in the Supporting Information. F 1s XPS spectrum presents two peaks related with different F local environments near to Li-F and Mn-F bonds, respectively, further confirming the successful F substitution in LMOF (Figure S1, Supporting Information).<sup>[13]</sup> Mn<sup>3+</sup> takes up  $\approx$  31% of total Mn amount, and the average valence state of Mn can be deduced as +3.69 (Figure S2, Supporting Information). Further combining with the elemental composition (Table S5, Supporting Information), the chemical formula of LMOF can be determined as Li<sub>0.87</sub>Mn<sub>0.80</sub>O<sub>1.81</sub>F<sub>0.19</sub>, highlighting the high F content of 9.5%. It indicates that, most of F substitution mainly occurred during the Li<sup>+</sup>/Na<sup>+</sup> ion-exchange process.

The local structure of LMOF was investigated by the highresolution transmission electron microscopy (HRTEM). HRTEM images for the near-surface region and the bulk were shown in Figure 1C; Figure S3, Supporting Information,

16136829, 2022, 6, Downloaded from https://onlinelibrary.wiley.com/doi/10.1002/smll.202103499 by University Town Of Shenzhen, Wiley Online Library on [24/11/2025]. See the Terms and Condition

nditions) on Wiley Online Library for rules of use; OA articles are governed by the applicable Creative Commons License

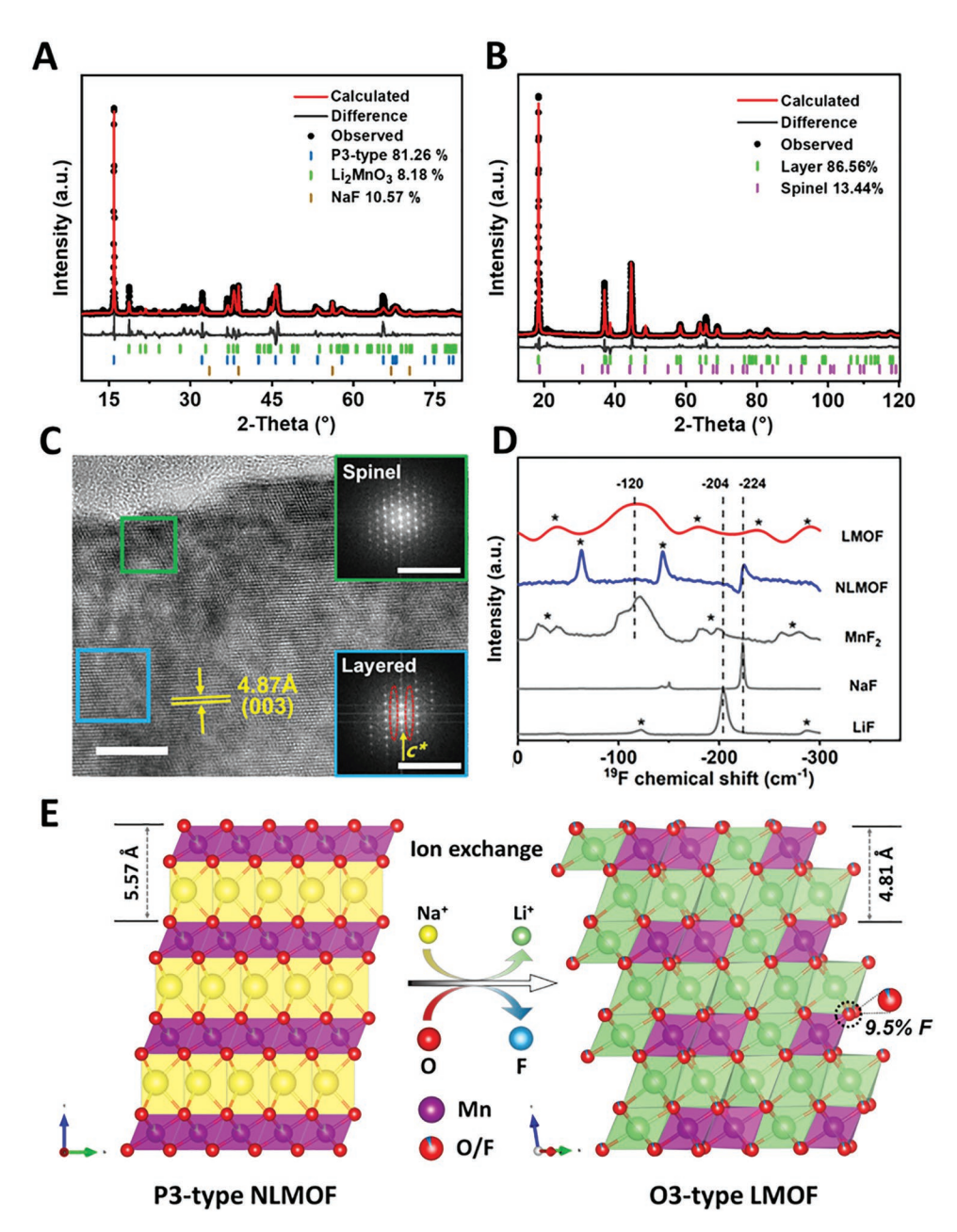


Figure 1. Structure analysis of NLMOF and LMOF. XRD pattern and Rietveld refinement result of A) NLMOF and B) LMOF. C) HRTEM image of LMOF at the near-surface region and the selected-area FFT patterns. The scale bars in HRTEM image and FFT maps are 10 nm and 10 1/nm, respectively. D) <sup>19</sup>F solid-state MAS (30 kHz) NMR spectra for as-prepared NMOF and LMOF, as well as the reference compounds LiF, NaF, and MnF<sub>2</sub>. The spinning sidebands are marked by the stars. The vertical dashed lines are used to mark the resonances for LiF, NaF, and MnF2, respectively. E) Schematic illustration of the ion-exchange process, including Li<sup>+</sup>/Na<sup>+</sup> exchange and F/O exchange.

respectively. The corresponding fast Fourier transform (FFT) map for the region marked by the green square demonstrates a typical spinel phase at the outmost surface. The layered (003) lattice fringe and the corresponding FFT map for the region marked by the blue square exhibit a layered main phase compositing with a little spinel phase, confirming a spinel shell coherently forming with the layered phase. The bulk of the LMOF particle presents a typical layered structure (Figure S3, Supporting Information), which is similar to that of Li<sub>2</sub>MnO<sub>3</sub> (Figure S4, Supporting Information). The interlayer spacing of LMOF is 4.87 Å, a little larger than that of Li<sub>2</sub>MnO<sub>3</sub> (4.83 Å), which is consistent with the shift of the corresponding peak to the lower angle for LMOF than that of Li<sub>2</sub>MnO<sub>3</sub> (Figure S5, Supporting Information), hinting the larger Li<sup>+</sup> slab and thus the better diffusion capability for LMOF. Such layered/spinel biphasic microstructure is in accordance with the results of XRD refinement. It may be ascribed to the heavy fluorination, since the previous reports indicated that, F substitution with a high content can induce the generation of spinel Li<sub>4</sub>Mn<sub>5</sub>O<sub>12</sub>.<sup>[8i]</sup> Such a spinel shell with a 3D Li<sup>+</sup> diffusion tunnels can improve

\_\_ small

www.advancedsciencenews.com

www.small-journal.com

16136282, 2022, 6, Downloaded from https://onlinelibrary.wiley.com/doi/10.1002/smll.202103499 by University Town of Shenzlen, Wiley Online Library on [24110205]. See the Terms and Conditions (https://onlinelibrary.wiley.com/terms-and-conditions) on Wiley Online Library for rules of use; OA articles are governed by the applicable Creative Commons Licenses, and Conditions (https://onlinelibrary.wiley.com/terms-and-conditions) on Wiley Online Library for rules of use; OA articles are governed by the applicable Creative Commons Licenses, and Conditions (https://onlinelibrary.wiley.com/terms-and-conditions) on Wiley Online Library for rules of use; OA articles are governed by the applicable Creative Commons Licenses, and Conditions (https://onlinelibrary.wiley.com/terms-and-conditions) on Wiley Online Library for rules of use; OA articles are governed by the applicable Creative Commons Licenses, and Conditions (https://onlinelibrary.wiley.com/terms-and-conditions) on Wiley Online Library for rules of use; OA articles are governed by the applicable Creative Commons Licenses, and the common of the

the Li+ diffusion ability at the surface. Furthermore, layered phase and spinel phase are coherently integrated at atomic scale, which can enhance the mechanical stability of surface structure, and avoid the falling off of the shell due to the lattice mismatch. HRTEM energy dispersive spectroscopy (EDS) mapping (Figure S6, Supporting Information) further confirms the homogeneous bulk substitution of F throughout the entire particle. To further examine the local structrue of F in LMOF, <sup>19</sup>F solid-state magic angle spin (MAS) nuclear magnetic resonance (NMR) spectra were acquired. As shown in Figure 1D, The resonance for NLMOF is located at -224 ppm, consistent with that of NaF. The result is in accordance with XRD refinement result, further confirming, F species in NLMOF exist in the form of the impurity NaF, not entering the layered lattice. As for LMOF, there is a broad peak centering around -120 ppm, which is basically consistent with the signal of MnF<sub>2</sub>. It arises from the strong paramagnetic interactions between F nuclei and the nearby Mn cations with unpaired d electrons.[10,14] We can conclude, F ions are integrated in the bulk lattice of LMOF in the form of Mn-F bonding. The broadening of <sup>19</sup>F signal in LMOF compared with that in MnF<sub>2</sub> may be due to multiple F local environments caused by layered/spinel composite structure or the difference at the surface and in the bulk. In addition, the absence of the sharp diamagnetic signal (-204 ppm) indicates that no LiF impurity is present in LMOF.

Based on the detailed structural analysis, the mechanism for the heavy fluorination through the ion-exchange route can be proposed (Figure 1E). In the precursor NLMOF, only a little amount of F enters the layered lattice, and most of F still exists in the form of NaF. During the ion-exchange process, Li ions completely replace Na ions, which induces the phase transition from P3 phase to O3 phase. In the meanwhile, lots of F enter into the anionic lattice to replace O anions. It should be related with the existence form of F species during the ion-exchange process. The phase diagram of LiF/LiNO3 (Figure S7, Supporting Information) indicates that, LiF would be in the form of the molten state when the mole ratio of LiNO<sub>3</sub>/(LiF+ LiNO<sub>3</sub>) exceeds 0.95. NaF has similar chemical properties with LiF. In the real synthesis process, the practical mole ratio of LiNO<sub>3</sub>/ (NaF+LiNO<sub>3</sub>) is above 0.95. Thus most of F ions exist in the form of molten state, making F ions enter into the anionic lattice to replace O anion easily.

In addition, SEM images were recorded to check the morphology of NLMOF, LMOF and Li<sub>2</sub>MnO<sub>3</sub> (Figure S8, Supporting Information). Similar prism-shape single crystal particles with the size of 1–10  $\mu m$  are observed for NLMOF and LMOF. It indicates that, the ion-exchange process has little influence on the particle morphology. The high-magnification SEM image along the side face of the particle (Figure S8D, Supporting Information) exhibits the lamellar stacking way for LMOF, which agrees well with the growth habit of the typical layered structure.

The electrochemical performance of LMOF was systemically tested in the half cells using Li foils as anodes. The charge/discharge curves at a current density of 10 mA  $\rm g^{-1}$  in 1.5–4.8 V are displayed in **Figure 2**A. LMOF can deliver an ultrahigh initial capacity of 389 mA h  $\rm g^{-1}$ , 85% of the theoretical capacity ( $\approx$ 460 mA h  $\rm g^{-1}$ ) of Li<sub>2</sub>MnO<sub>3</sub>. By comparison, Li<sub>2</sub>MnO<sub>3</sub> delivers a much lower discharge capacity of 134 mA h  $\rm g^{-1}$  in the first cycle

(Figure S9, Supporting Information). The initial Coulombic efficiency is over 100% (≈160%) owing to Li-deficient character of LMOF. And the initial charge capacity of 225 mA h g<sup>-1</sup> nearly matches the theoretical value (≈280 mA h g<sup>-1</sup>) deduced from the chemical formula Li<sub>0.87</sub>Mn<sub>0.80</sub>O<sub>1.81</sub>F<sub>0.19</sub>. The capacity contributed by the spinel component can be estimated as 30 mA h g<sup>-1</sup> during the first charge (Figure S10, Supporting Information), about 13% of the first charge capacity, consistent with the refinement result above. To analyze the detailed redox reactions during the charge/discharge, the corresponding dQ/dV curves are shown in Figure 2B. According to the peak positions, the charge/discharge curves can be divided into three sections, the region below 2.4 V, the redox peaks at around 3.05 V (marked by the cyan shade), and the region above 3.9 V (marked by the purple shade). The former two regions come from Mn<sup>3+</sup>/Mn<sup>4+</sup> couple. The third region belongs to oxygen redox. During the first charge, a sharp peak appeared at 4.64 V. It evolves to a broad peak in 3.9-4.8 V in the subsequent cycles, which steadily occurs until the tenth cycle, indicating the good reversibility of oxygen redox.

As shown in Figure 2D, LMOF achieves superior rate performance at different current densities. The discharge capacities are 386, 323, 280, 235, 176, 135, and 98 mA h g<sup>-1</sup> at 20, 50, 100, 200, 500, 1000, 2000 mA g<sup>-1</sup>, respectively (Figure S11, Supporting Information). Such good rate capability might benefit from the 3D Li<sup>+</sup> diffusion channels in the spinel shell. The cycling stability was also evaluated at 10 and 50 mA g<sup>-1</sup> (Figure 2C,E). Surprisingly, LMOF has a good capacity retention of 93.7%, and a low voltage fading of about 0.121 V after 30 cycles at 10 mA g<sup>-1</sup>. Accordingly, a very high energy density up to 1150 W h kg-1 with good reversibility is achieved (Figure S12, Supporting Information), which is higher than traditional Li-rich layered cathode materials (≈900 W h kg<sup>-1</sup>). When cycled at a higher current of 50 mA g<sup>-1</sup>, LMOF also delivers a large capacity retention of 91.8% and a low voltage decay of 0.221 V after 120 cycles (Figure 2E), while Li<sub>2</sub>MnO<sub>3</sub> only delivers a capacity of 124 mA h g-1 with the retention of 57.9% (Figure S13, Supporting Information). To our knowledge, integrating the high discharge capacity and the good cycling stability, LMOF exhibits the best performance among all reported F-doping oxide cathode materials for LIBs (Tables S1 and S2, Supporting Information).

Such excellent electrochemical performance can be ascribed to the high-proportion F substitution of O. When charging to high potentials (>4.0 V), the presence of strong Mn—F bond can greatly prohibit Mn migration to adjacent Li vacancies and hence the formation of molecular O<sub>2</sub> on deep charge, which can stabilize the layered lattice structure by suppressing irreversible oxygen loss and the formation of spinel-like phase (Scheme 1A). When cycling at low potentials (<3.0 V), the F<sup>-</sup>/O<sup>2-</sup> mixed anions can break the electronic symmetry around Mn<sup>3+</sup> to reduce the Jahn–Teller distortion, and enhancing the cycling stability.<sup>[10]</sup> Additionally, the surface spinel shell plays an important role in protecting electrode from attacking by acidic species and alleviating Mn dissolution.

To investigate the charge compensation mechanism, Mn 2p and O 1s XPS spectra were collected on the LMOF electrodes at different charge/discharge states during the first two cycles (Figure 3A). As shown in Figure S14 in the Supporting

16136829, 2022, 6, Downloaded from https://onlinelibrary.wiley.com/doi/10.1002/smll.202103499 by University Town Of Shenzhen, Wiley Online Library on [24/11/2025]. See the Terms

litions) on Wiley Online Library for rules of use; OA articles are governed by the applicable Creative Commons License

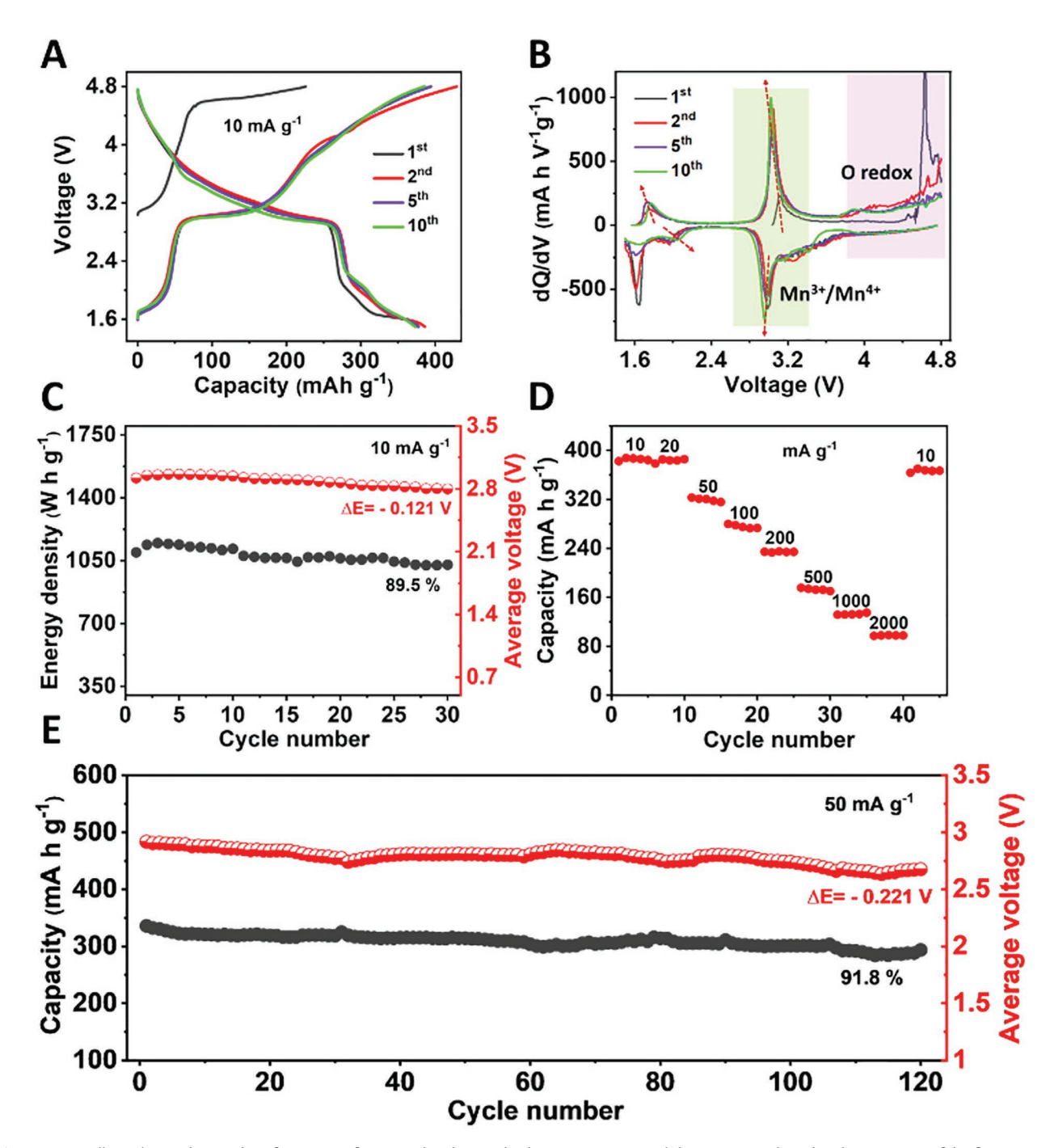


**Figure 2.** Excellent electrochemical performance of LMOF. The charge/discharge curves A) and the corresponding dQ/dV curves B) of the first, second, fifth, and tenth cycle at a rate of 10 mA  $g^{-1}$ . The red arrows are used to indicate the trend of peak changes. C) Plot of the discharge capacity and average discharge potential versus cycle number at a rate of 10 mA  $g^{-1}$ . D) The rate capacity of LMOF at different current densities varying from 10 to 2000 mA  $g^{-1}$ . E) Plot of the discharge capacity and the average discharge potential versus cycle number at a rate of 50 mA  $g^{-1}$ .

Information, the Mn  $2p_{3/2}$  peak was fitted individually for each spectrum, and Mn average valence was plotted as a function of the charge/discharge state in Figure 3B. In pristine LMOF, the average valence of Mn is +3.69. The lower valence of Mn can be ascribed to the introduction of the low-valent F ion. When charged to 4.0 V, Mn is oxidized to +3.82. It indicates that, the capacity below 4 V mainly comes from the contribution of

Mn<sup>3+</sup>/Mn<sup>4+</sup> redox couple. When further charged to 4.6 V, partial reduction of Mn is observed, which hints the oxygen redox in this region.<sup>[15]</sup> Even further charged to 4.8 V and discharged to 3.5 V, Mn valence state keeps nearly constant. It signifies that, oxygen redox dominates in the voltage region and prevents the fully oxidation of Mn to +4 (marked by the purple shade), which could be due to more overlap between Mn and O redox induced

16136829, 2022, 6, Downloaded from https://onlinelibrary.wiley.com/doi/10.1002/smll.202103499 by University Town Of Shenzhen, Wiley Online Library on [24/112025]. See the Terms and Condition

ns (https://onlinelibrary.wiley.com/tern

and-conditions) on Wiley Online Library for rules of use; OA articles are governed by the applicable Creative Commons License

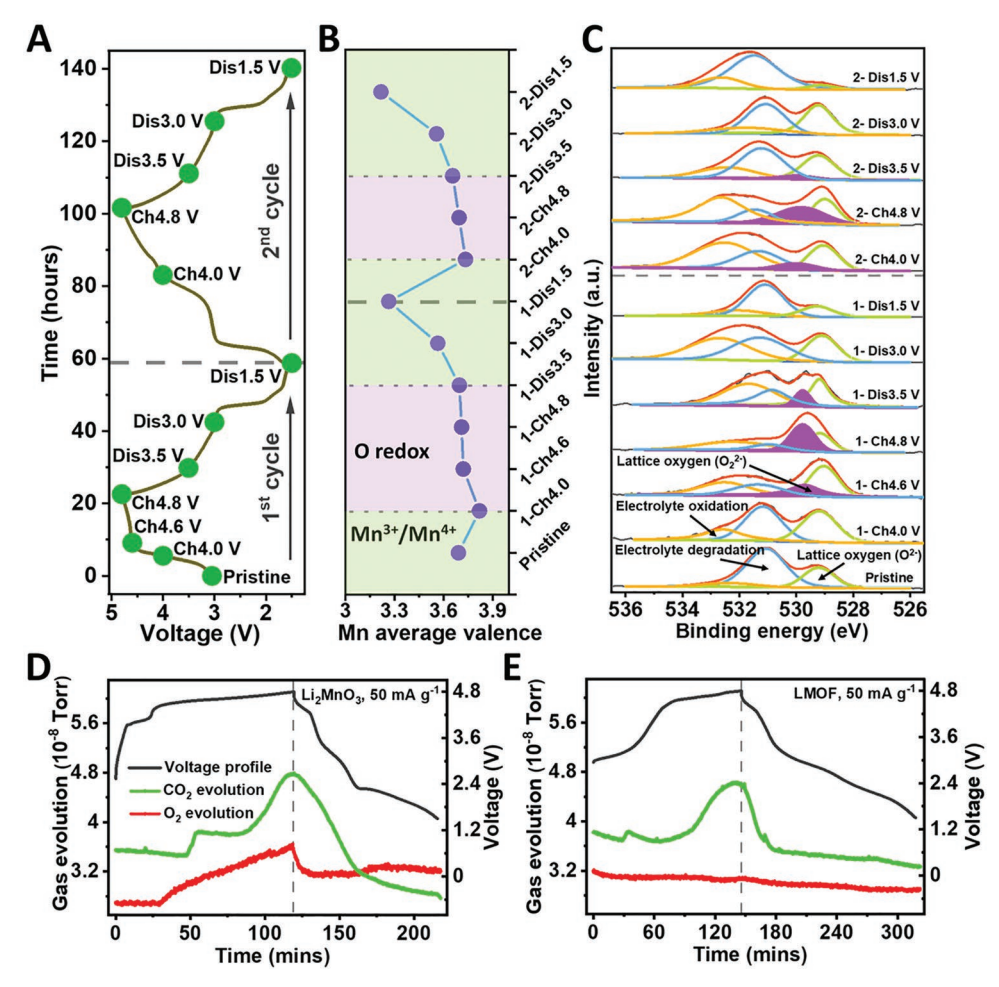


Figure 3. Reversible anionic redox by heavy fluorination. A) The charge/discharge curves during the first two cycles of LMOF, and the selected charge/ discharge points to measure the XPS spectra (marked by green spots). Evolution of Mn average valence (B) and O 1s XPS spectra (C) of LMOF at selected charge/discharge states in A. Operando DEMS results for Li<sub>2</sub>MnO<sub>3</sub> (D) and LMOF (E) during the first cycle.

by the F substitution.<sup>[14d,16]</sup> As the discharge continues below 3.5 V, Mn cations start to be reduced and fast go down to an average valence of +3.26 till 1.5 V. The similar change trend of Mn valence can be observed during the second cycle. To further confirm the involvement of reversible oxygen redox, O 1s spectra were also fitted in Figure 3C. In the pristine sample, there is a strong peak at 529.2 eV from lattice oxygen, whereas the other peak at 531 eV comes from the electrolyte degradation. When charged to 4.6 V, a new peak appears at 529.9 eV (purple), which can be attributed to the existence of formal  $O_2^{2-}$ species.<sup>[17]</sup> The O<sub>2</sub><sup>2-</sup> peak increases when charged to 4.8 V, and gradually decreases when discharged to 3.5 V, eventually disappears when discharged to 3.0 V, which corresponds to the constant Mn valence state in the same voltage region (Figure 3B). It indicates that, the oxygen redox activity is important to realize the high capacity for LMOF. During the second cycle, the  $O_2^{2-}$ peak at 529.9 eV reappears at 4.0 V and disappears till 3.0 V, further confirming the high reversibility of oxygen redox.

In order to evaluate the influences of heavy fluorination on the irreversible side reactions and the oxygen evolution, operando differential electrochemical mass spectrometry (DEMS) measurements were performed on LMOF and Li<sub>2</sub>MnO<sub>3</sub>

during the first cycle (Figure 3D,E). Upon the first charge, a mass of O<sub>2</sub> release is detected above 4.5 V in Li<sub>2</sub>MnO<sub>3</sub>, accompanying with much CO2 release above 4.6 V. It indicates the irreversible oxygen redox and the serious side reactions with the electrolyte. In sharp contrast, there is negligible O2 gas and also the decreased CO<sub>2</sub> release for LMOF, indicating the high reversibility of oxygen redox and the suppressed side reactions for LMOF. Since CO2 evolution originates from surface carbonate decomposition (e.g., Li<sub>2</sub>CO<sub>3</sub>) and the electrolyte oxidized by oxygen radicals at high potentials,[16,18] it is rational to see the less CO2 release with highly reversible oxygen redox in LMOF. These results prove that heavy fluorination substantially mitigates oxygen loss arising from the formation of brisk molecular O2 on the deep charge. [19] The less surface side reactions in LMOF than in  $\text{Li}_2\text{MnO}_3$  can also be partially ascribed to the protection of the spinel shell.

Ex situ XRD was carried out to investigate the detailed structural evolution of LMOF during the first cycle. To avoid the experimental error, all the patterns were calibrated using the main peak of Al current collectors at around 65°. As shown in Figure 4A, there is an obvious peak shift to higher angle when charging from 4.6 to 4.8 V. It is consistent with the previous

16136829, 2022, 6, Downloaded from https://onlinelibrary.wiley.com/doi/10.1002/smll.202103499 by University Town Of Shenzhen, Wiley Online Library on [24/11/2025]. See the Term

ons) on Wiley Online Library for rules of use; OA articles are governed by the applicable Creative Commons Licens

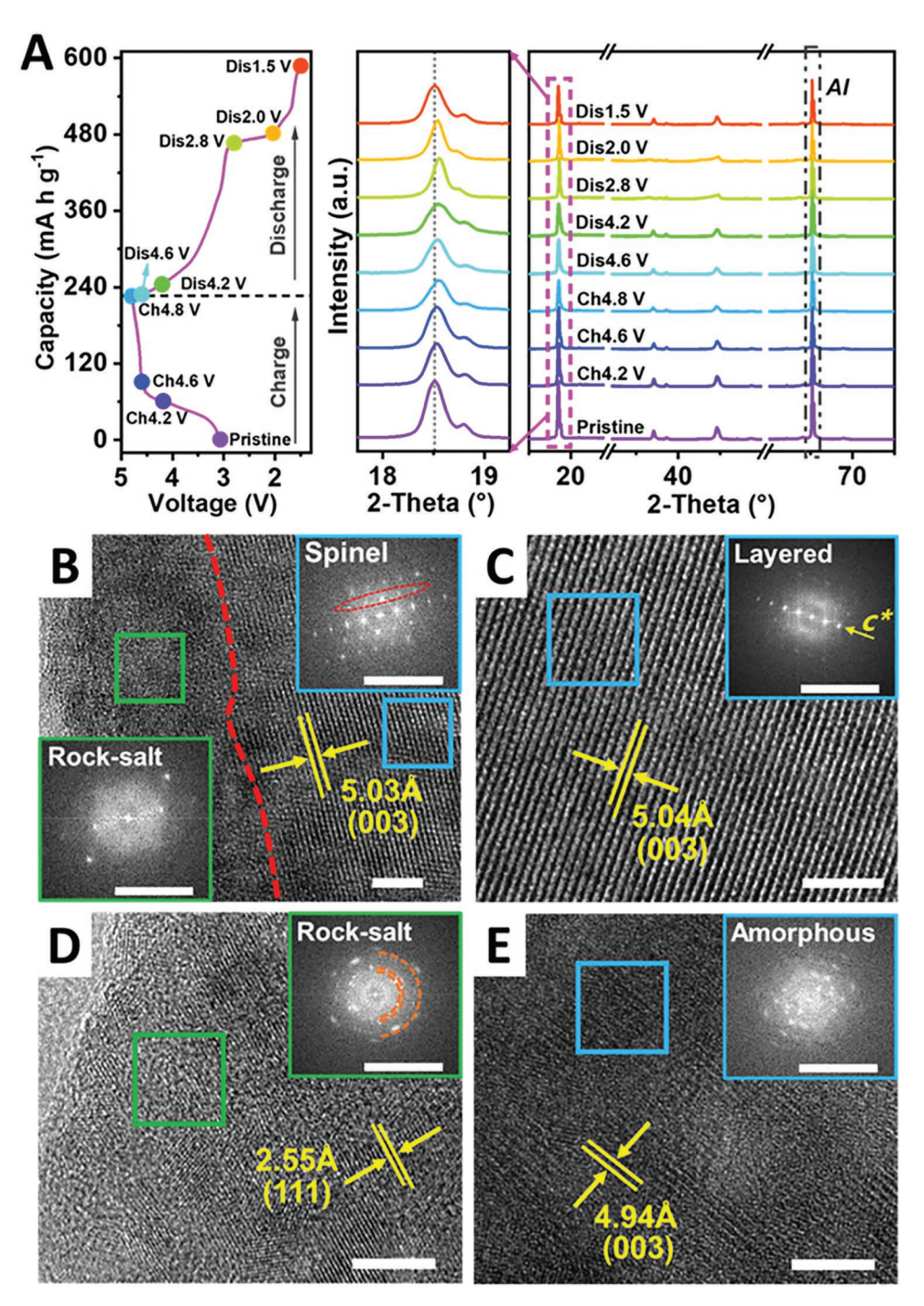


Figure 4. Enhanced structural stability of LMOF upon cycling. A) Ex situ XRD patterns for LMOF during the first cycle. The left panel shows the corresponding charge/discharge profile with the points where XRD patterns were collected. HRTEM images and the selected-region FFT patterns at the particle surface (B) and in the bulk (C) of LMOF after 120 cycles. HRTEM images and the selected-region FFT patterns at the particle (D) and in the bulk (E) of  $Li_2MnO_3$  after 120 cycles. The scale bars in HRTEM images and the FFT maps are 5 nm and 10 1/nm, respectively.

reports, and ascribed to the formation of the lattice O<sup>-</sup> species, which decreases the interlayer repulsion, thus reducing the interlayer distance.<sup>[20]</sup> When discharging to 1.5 V, the main peak returns to the primal position before cycling, indicating the reversible structure change.

Local structural evolution was furtherly studied by HRTEM images and FFT patterns. Figure 4B,C presents HRTEM

images of LMOF at the particle surface and in the bulk after 120 cycles, respectively. The outmost surface with the thickness around 20 nm is the rock-salt phase, and the inner surface still preserves the layered/spinel composite structure. The bulk maintains the well layered structure, confirmed by the clear lattice fringes with d-spacing 5.04 Å. The superficial rock-salt phase mainly transforms from the initial spinel

www.advancedsciencenews.com



16136282, 2022, 6, Downloaded from https://onlinelibrary.wiley.com/doi/10.1002/smll.202103499 by University Town of Shenzlen, Wiley Online Library on [24110205]. See the Terms and Conditions (https://onlinelibrary.wiley.com/terms-and-conditions) on Wiley Online Library for rules of use; OA articles are governed by the applicable Creative Commons Licenses, and Conditions (https://onlinelibrary.wiley.com/terms-and-conditions) on Wiley Online Library for rules of use; OA articles are governed by the applicable Creative Commons Licenses, and Conditions (https://onlinelibrary.wiley.com/terms-and-conditions) on Wiley Online Library for rules of use; OA articles are governed by the applicable Creative Commons Licenses, and Conditions (https://onlinelibrary.wiley.com/terms-and-conditions) on Wiley Online Library for rules of use; OA articles are governed by the applicable Creative Commons Licenses, and Conditions (https://onlinelibrary.wiley.com/terms-and-conditions) on Wiley Online Library for rules of use; OA articles are governed by the applicable Creative Commons Licenses, and the common of the

www.small-journal.com

shell, suggesting that, the original spinel shell of LMOF effectively protects the bulk structure upon long-term cycling. In contrast, Li<sub>2</sub>MnO<sub>3</sub> sample suffers terrible structural degradation. The surface completely degrades to the rock-salt phase (Figure 4D), and the bulk transforms to the amorphous state to a great extent (Figure 4E). The severe structural degradation originates from irreversible Mn migration and serious oxygen loss at high voltages (Scheme 1A). [6a,19a,21] These comparative observations forcefully support that, heavy fluorination effectively stabilizes the layered anionic lattice, and greatly suppresses the structure degradation, thus enhancing long-term cycling stability by introducing strong Mn—F bonds and the coherent spinel shell.

#### 3. Conclusion

In summary, heavy fluorination up to 9.5 at% was successfully implemented in the layered Li-Mn-O system through a unique ion-exchange route. F substitution of O improves the stability of the layered anionic framework, completely inhibits the O2 evolution during the first cycle, and greatly enhances the reversibility of oxygen redox, delivering an ultrahigh reversible capacity of 389 mA h g<sup>-1</sup>, 85% of the theoretical capacity of Li<sub>2</sub>MnO<sub>3</sub> (≈460 mA h g<sup>-1</sup>). Moreover, heavy fluorination also induces a spinel shell coherently forming on the particle surface, which greatly improves the surface structure stability and the Li<sup>+</sup> diffusivity, making LMOF exhibit a superior cycling stability (a capacity retention of 91.8% after 120 cycles at 50 mA g<sup>-1</sup>) and a good rate capability. These findings stress the importance of stabilizing the layered anionic framework in developing highperformance low-cost cathodes for next-generation Li-ion batteries.

### **Supporting Information**

Supporting Information is available from the Wiley Online Library or from the author.

### **Acknowledgements**

The authors acknowledge support from the Soft Science Research Project of Guangdong Province (2017B030301013), the Shenzhen Science and Technology Research Grant (No. JCYJ20200109140416788), the Chemistry and Chemical Engineering Guangdong Laboratory (Grant No.1922018), and the National Key R&D Program of China (2020YFB0704500).

### **Conflict of Interest**

The authors declare no conflict of interest.

## **Data Availability Statement**

The data that supports the findings of this study are available in the supplementary material of this article.

## **Keywords**

anionic frameworks, heavy fluorination, Li-ion batteries, lithium manganese layered oxide, reversible oxygen redox

Received: June 22, 2021 Revised: October 15, 2021 Published online: December 1, 2021

- [1] M. Armand, J. M. Tarascon, Nature 2008, 451, 652.
- [2] a) A. Manthiram, Nat. Commun. 2020, 11, 1550; b) F. Wu, J. Maier, Y. Yu, Chem. Soc. Rev. 2020, 49, 1569.
- [3] a) L. Li, K. S. Lee, L. Lu, Funct. Mater. Lett. 2014, 7, 1430002;
   b) P. Rozier, J. M. Tarascon, J. Electrochem. Soc. 2015, 162, A2490.
- [4] a) R. Wang, X. He, L. He, F. Wang, R. Xiao, L. Gu, H. Li, L. Chen, Adv. Energy Mater. 2013, 3, 1358; b) D. Ye, G. Zeng, K. Nogita, K. Ozawa, M. Hankel, D. J. Searles, L. Wang, Adv. Funct. Mater. 2015, 25, 7488.
- [5] a) E. Cho, K. Kim, C. Jung, S.-W. Seo, K. Min, H. S. Lee, G.-S. Park, J. Shin, J. Phys. Chem. C 2017, 121, 21118; b) A. Marusczyk, J.-M. Albina, T. Hammerschmidt, R. Drautz, T. Eckl, G. Henkelman, J. Mater. Chem. A 2017, 5, 15183.
- [6] a) P. Yan, L. Xiao, J. Zheng, Y. Zhou, Y. He, X. Zu, S. X. Mao, J. Xiao, F. Gao, J.-G. Zhang, C.-M. Wang, Chem. Mater. 2015, 27, 975;
  b) S.-H. Park, Y. Sato, J.-K. Kim, Y.-S. Lee, Mater. Chem. Phys. 2007, 102, 225;
  c) M. Gu, I. Belharouak, J. Zheng, H. Wu, J. Xiao, A. Genc, K. Amine, S. Thevuthasan, D. R. Baer, J.-G. Zhang, N. D. Browning, J. Liu, C. Wang, ACS Nano 2013, 7, 760.
- [7] a) S.-J. Kim, M.-C. Kim, D.-H. Kwak, D.-M. Kim, G.-H. Lee, H.-S. Choe, K.-W. Park, J. Power Sources 2016, 304, 119; b) F. Wang, Z. Chang, X. Wang, Y. Wang, B. Chen, Y. Zhu, Y. Wu, J. Mater. Chem. A 2015, 3, 4840; c) A. Klein, P. Axmann, C. Yada, M. Wohlfahrt-Mehrens, J. Power Sources 2015, 288, 302; d) W. Zhao, L. Xiong, Y. Xu, H. Li, Z. Ren, J. Power Sources 2017, 349, 11.
- [8] a) L. Torres-Castro, M. A. Abreu-Sepulveda, R. S. Katiyar, A. Manivannan, J. Electrochem. Soc. 2017, 164, A1464; b) Y. Xiang, X. Wu, Ionics 2018, 24, 83; c) W. Zhao, L. Xiong, Y. Xu, X. Xiao, J. Wang, Z. Ren, J. Power Sources 2016, 330, 37; d) K. W. Kang, Y. U. Jeong, Y. J. Lee, J. Ceram. Proc. Res. 2016, 17, 54; e) M. Tabuchi, H. Kageyama, K. Takamori, Y. Imanari, K. Nakane, Electrochim. Acta 2016, 210, 105; f) O. M. Ozkendir, M. Harfouche, I. Ulfat, C. Kaya, G. Celik, S. Ates, S. Aktas, H. Bavegar, T. Colak, J. Electron Spectrosc. Relat. Phenom. 2019, 235, 23; g) Y. Gao, J. Ma, X. Wang, X. Lu, Y. Bai, Z. Wang, L. Chen, J. Mater. Chem. A 2014, 2, 4811; h) Z. Q. Wang, M. S. Wu, B. Xu, C. Y. Ouyang, J. Alloys Compd. 2016, 658, 818; i) X. Dong, Y. Xu, S. Yan, S. Mao, L. Xiong, X. Sun, J. Mater. Chem. A 2015, 3, 670; j) J. C. Im, N. H. Vu, H. T. Huu, D. S. H. Lee, W. B. Im, J. Electrochem. Soc. 2019, 166, A1568.
- [9] a) M. Cheng, K. Zhu, L. Yang, L. Zhu, Y. Li, W. Tang, J. Alloys Compd.
  2016, 686, 496; b) G. Yang, L. Wang, J. Wang, W. Yan, Ceram. Int. 2017, 43, 71; c) M. Cheng, W. Tang, Y. Sun, K. Zhu, RSC Adv.
  2015, 5, 71088; d) M. Diaz-Lopez, P. A. Chater, Y. Joly, O. Proux, J.-L. Hazemann, P. Bordet, V. Pralong, J. Mater. Chem. A 2020, 8, 10998; e) M. Freire, O. I. Lebedev, A. Maignan, C. Jordy, V. Pralong, J. Mater. Chem. A 2017, 5, 21898; f) R. Kataoka, N. Taguchi, T. Kojima, N. Takeichi, T. Kiyobayashi, J. Mater. Chem. A 2019, 7, 5381.
- [10] Z. Lun, B. Ouyang, D. A. Kitchaev, R. J. Clément, J. K. Papp, M. Balasubramanian, Y. Tian, T. Lei, T. Shi, B. D. McCloskey, J. Lee, G. Ceder, Adv. Energy Mater. 2019, 9, 1802959.
- [11] J. A. Dean, N. A. Lange, Lange's Handbook of Chemistry, 15th ed., McGraw-Hill, New York 1998.
- [12] J. Ahn, D. Chen, G. Chen, Adv. Energy Mater. 2020, 10, 2001671.

SMQ

16136829, 2022, 6, Downloaded from https://onlinelibrary.wiley.com/doi/10.1002/smll.202103499 by University Town Of Shenzhen, Wiley Online Library on [24/11/2025]. See the Terms

and Conditions

(https://onlinelibrary.wiley.com

and-conditions) on Wiley Online Library for rules of use; OA articles are governed by the applicable Creative Commons Licenses

www.advancedsciencenews.com www.small-journal.com

- [13] D. Luo, X. K. Ding, J. M. Fan, Z. H. Zhang, P. Z. Liu, X. H. Yang, J. J. Guo, S. H. Sun, Z. Lin, Angew. Chem., Int. Ed. 2020, 59, 23061
- [14] a) J. Y. Lee, J. K. Papp, R. J. Clement, S. Sallis, D. H. Kwon, T. Shi, W. L. Yang, B. D. McCloskey, G. Ceder, Nat. Commun. 2017, 8, 981;
  b) R. Y. Chen, S. H. Ren, M. Knapp, D. Wang, R. Witter, M. Fichtner, H. Hahn, Adv. Energy Mater. 2015, 5, 1401814; c) R. A. House, L. Y. Jin, U. Maitra, K. Tsuruta, J. W. Somerville, D. P. Forstermann, F. Massel, L. Duda, M. R. Roberts, P. G. Bruce, Energy Environ. Sci. 2018, 11, 926; d) Z. Lun, B. Ouyang, Z. Cai, R. J. Clément, D.-H. Kwon, J. Huang, J. K. Papp, M. Balasubramanian, Y. Tian, B. D. McCloskey, H. Ji, H. Kim, D. A. Kitchaev, G. Ceder, Chem 2020, 6, 153.
- [15] M. Sathiya, G. Rousse, K. Ramesha, C. P. Laisa, H. Vezin, M. T. Sougrati, M. L. Doublet, D. Foix, D. Gonbeau, W. Walker, A. S. Prakash, M. Ben Hassine, L. Dupont, J. M. Tarascon, *Nat. Mater.* 2013, 12, 827.
- [16] J. Lee, D. A. Kitchaev, D.-H. Kwon, C.-W. Lee, J. K. Papp, Y.-S. Liu, Z. Lun, R. J. Clément, T. Shi, B. D. McCloskey, J. Guo, M. Balasubramanian, G. Ceder, *Nature* 2018, 556, 185.
- [17] E. McCalla, A. M. Abakumov, M. Saubanere, D. Foix, E. J. Berg, G. Rousse, M.-L. Doublet, D. Gonbeau, P. Novak, G. Van Tendeloo, R. Dominko, J.-M. Tarascon, *Science* 2015, 350, 1516.
- [18] R. Imhof, P. Novák, J. Electrochem. Soc. 1999, 146, 1702.

- [19] a) A. R. Armstrong, M. Holzapfel, P. Novák, C. S. Johnson, S.-H. Kang, M. M. Thackeray, P. G. Bruce, J. Am. Chem. Soc. 2006, 128, 8694; b) R. A. House, U. Maitra, L. Jin, J. G. Lozano, J. W. Somerville, N. H. Rees, A. J. Naylor, L. C. Duda, F. Massel, A. V. Chadwick, S. Ramos, D. M. Pickup, D. E. McNally, X. Lu, T. Schmitt, M. R. Roberts, P. G. Bruce, Chem. Mater. 2019, 31, 3293.
- [20] a) J. L. Shi, J. N. Zhang, M. He, X. D. Zhang, Y. X. Yin, H. Li, Y. G. Guo, L. Gu, L. J. Wan, ACS Appl. Mater. Interfaces 2016, 8, 20138; b) S. Shen, Y. Hong, F. C. Zhu, Z. M. Cao, Y. Y. Li, F. S. Ke, J. J. Fan, L. L. Zhou, L. N. Wu, P. Dai, M. Z. Cai, L. Huang, Z. Y. Zhou, J. T. Li, Q. H. Wu, S. G. Sun, ACS Appl. Mater. Interfaces 2018, 10, 12666; c) Y. X. Cai, L. Ku, L. S. Wang, Y. T. Ma, H. F. Zheng, W. J. Xu, J. T. Han, B. H. Qu, Y. Z. Chen, Q. S. Xie, D. L. Peng, Sci. China Mater. 2019, 62, 1374; d) Z. Li, Y. Li, M. Zhang, Z.-W. Yin, L. Yin, S. Xu, C. Zuo, R. Qi, H. Xue, J. Hu, B. Cao, M. Chu, W. Zhao, Y. Ren, L. Xie, G. Ren, F. Pan, Adv. Energy Mater. 2021, 11, 101962. e) J. Lee, D.-H. Seo, M. Balasubramanian, N. Twu, X. Li, G. Ceder, Energy Environ. Sci. 2015, 8, 3255.
- [21] a) W. E. Gent, K. Lim, Y. Liang, Q. Li, T. Barnes, S.-J. Ahn, K. H. Stone, M. McIntire, J. Hong, J. H. Song, Y. Li, A. Mehta, S. Ermon, T. Tyliszczak, D. Kilcoyne, D. Vine, J.-H. Park, S.-K. Doo, M. F. Toney, W. Yang, D. Prendergast, W. C. Chueh, Nat. Commun. 2017, 8, 2091; b) M. Zhang, Z. Li, L. Yu, D. Kong, Y. Li, B. Cao, W. Zhao, J. Wen, F. Pan, Nano Energy 2020, 77, 105188.